Lateral spectrum splitting system with perovskite photovoltaic cells

Benjamin D. Chrysler,[a,*] **Sean E. Shaheen,**[b,c,d] **and Raymond K. Kostuk**[a,e]
[a]University of Arizona, James C. Wyant College of Optical Sciences,
Tucson, Arizona, United States
[b]University of Colorado Boulder, Department of Electrical, Computer, and Energy Engineering,
Boulder, Colorado, United States
[c]University of Colorado Boulder, Department of Physics, Boulder, Colorado, United States
[d]University of Colorado Boulder, Renewable and Sustainable Energy Institute,
Boulder, Colorado, United States
[e]University of Arizona, Department of Electrical and Computer Engineering,
Tucson, Arizona, United States

Abstract. We examine the potential of a multijunction spectrum-splitting photovoltaic (PV) solar energy system with perovskite PV cells. Spectrum splitting allows combinations of different energy band gap PV cells that are laterally separated and avoids the complications of fabricating tandem stack architectures. Volume holographic optical elements have been shown to be effective for the spectrum-splitting operation and can be incorporated into compact module packages. However, one of the remaining issues for spectrum splitting systems is the availability of low-cost wide band gap and intermediate band gap cells that are required for realizing high overall conversion efficiency. Perovskite PV cells have been fabricated with a wide range of band gap energies that potentially satisfy the requirements for multijunction spectrum-splitting systems. A spectrum-splitting system is evaluated for a combination of perovskite PV cells with energy band gaps of 2.30, 1.63, and 1.25 eV and with conversion efficiencies of 10.4%, 21.6%, and 20.4%, respectively, which have been demonstrated experimentally in the literature. First, the design of a cascaded volume holographic lens for spectral separation in three spectral bands is presented. Second, a rigorous coupled wave model is developed for computing the diffraction efficiency of a cascaded hologram. The model accounts for cross-coupling between higher diffraction orders in the upper and lower holograms, which previous models have not accounted for but is included here with the experimental verification. Lastly, the optical losses in the system are analyzed and the hypothetical power conversion efficiency is calculated to be 26.7%. *© 2022 Society of Photo-Optical Instrumentation Engineers (SPIE)* [DOI: 10.1117/1.JPE.12.022206]

Keywords: photovoltaics; spectrum splitting; perovskites; holography; diffraction; multijunction; cascaded hologram; rigorous coupled wave analysis.

Paper 22008SS received Jan. 22, 2022; accepted for publication Apr. 27, 2022; published online May 18, 2022.

1 Introduction

Lateral spectrum splitting is a technique for increasing the conversion efficiency of a photovoltaic (PV) system. In a lateral spectrum-splitting photovoltaic (SSPV) system, an optical filter such as a dichroic filter or a diffraction grating is used to divide the solar spectrum between a set of single-junction PV cells with different band gap energies[1] [Fig. 1(a)]. One of the main limitations of lateral SSPV systems is the availability of inexpensive wide-band gap PV cells.

A new class of perovskite materials for PV cell applications has rapidly developed in the past decade. Perovskite solar cells (PSCs) have been demonstrated with band gap energies ranging between 1.25 eV and 2.30 eV making them good candidates for use in SSPV systems.[2–4] In addition to a variety of energy band gaps, PSCs are inexpensive[5] and have conversion

---

[*] Address all correspondence to Benjamin D. Chrysler, bc.chrysler@gmail.com

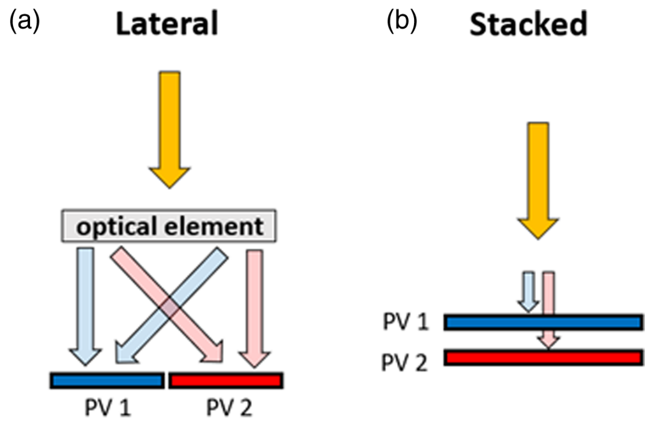

Fig. 1 Illustration of two different configurations for multijunction PV systems: (a) lateral spectrum splitting and (b) tandem cell stack.

efficiencies up to 25.5%.[6,7] As shown in the literature, multijunction PSC systems have been implemented as vertically stacked cells in a tandem module configuration[8–10] [Fig. 1(b)]. However, to the authors' knowledge, lateral spectrum splitting configurations using PSCs have not been demonstrated or studied in detail. In a tandem configuration, the cell on the top of the stack converts the shorter wavelength light, and the cell on the bottom converts longer wavelength light. Optimal band gaps for each were demonstrated in a perovskite/perovskite, four-terminal tandem device with 20.5% conversion efficiency.[8] More recently, a 24.2% conversion efficiency was confirmed for a perovskite/perovskite two-terminal tandem cell using a combination of 1.22 and 1.77 eV PSCs.[7,9]

Two-terminal, vertically stacked tandems are the focus of most efforts due to their relative simplicity.[9,10] However, the lateral spectrum splitting arrangement has several advantages that make it attractive for implementing multijunction systems, such as reduced parasitic absorption, greater solar cell design flexibility, and reduced PV cell material usage. Parasitic absorption is less in a lateral SSPV arrangement than vertically stacked tandem cells since the optical filter sends each spectral band directly to the individual PV cells without transmitting through multiple transparent conductive oxide layers that absorb sunlight.[4,9–14] A second advantage of a lateral spectrum splitting configuration is fewer constraints on the solar cell design. In a vertically stacked cell arrangement, the spectrum of light transmitted through the top cell must be considered in the design process since it affects the conversion efficiency of the bottom cell.[14] This in turn limits the design of the electrodes, antireflection coatings, rear reflector, and absorber. In a lateral SSPV system, however, these design aspects can be independently optimized since each cell receives sunlight directly from the optical filter without transmission through other cells. Furthermore, recent advancements in perovskite deposition techniques provide a potential route for manufacturing lateral SSPV systems with PSCs.[15] One of the most common, slot-die coating, allows for deposition of cells ∼1 cm across on flexible substrates such as plastic, stainless steel, or thin glass.[16] This technique could be extended by developing a head with multiple, offset slots for depositing different materials on a common substrate.[17] Alternatively, a single head with the ability to deposit different materials could be developed.

Despite the potential advantages of the lateral SSPV configuration, it remains a challenge to design a module with both high conversion efficiency and a form factor comparable to conventional flat-panel modules. One potential approach uses a volume holographic lens (VHL) array to disperse light onto rectangular shaped PV cells.[18] Light at a transition wavelength focuses in one dimension to the boundary between two adjacent PV cells. The transition wavelength is selected to be equal to the band gap wavelength of the wide-band gap cell, and once this is established the hologram is designed based on the Bragg condition and the grating equation.[18] Light at longer wavelengths disperse across the narrow-band gap cell, and light at shorter wavelengths disperse across the wide-band gap cell. The VHL module also converts diffuse sunlight and can be integrated in a single-axis sun tracking system.[18,19] Roll-to-roll manufacturing processes have been demonstrated by Prism Solar[20] with costs as low as \$2 to \$3/m^2. The small added cost may be

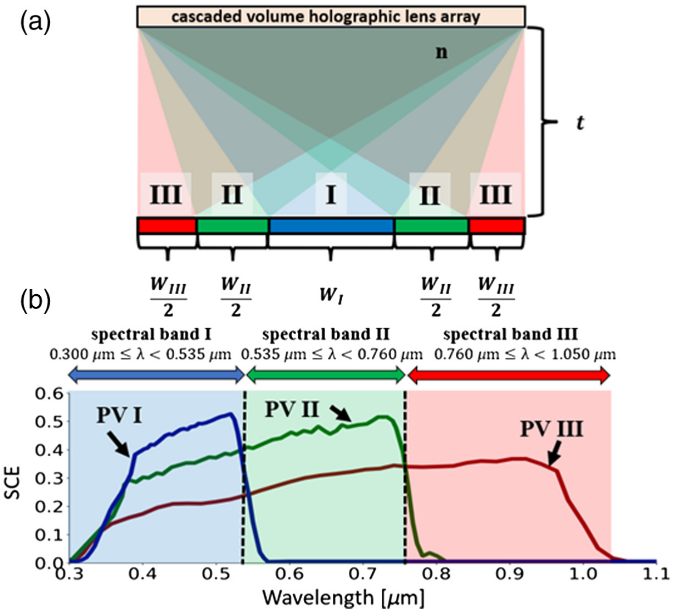

Fig. 2 (a) Unit cell for a three-bandgap lateral spectrum-splitting system. (b) SCE for the three perovskite cells used in the spectrum-splitting system.

justified by the increased conversion efficiency when considering the higher estimated manufacturing cost for a PSC (\$7 to \$11/m^2).[21,22] However, this approach has only been demonstrated with two band gaps, and it would be beneficial to incorporate the wider range of energy band gaps afforded by perovskites into a spectrum splitting design.

In this paper, a lateral SSPV system is proposed that uses a cascaded volume holographic lens array (CVHLA) for splitting the solar spectrum between three PSCs. The module consists of an array of unit cells as depicted in Fig. 2(a). The CVHLA is designed for fabrication in the dichromated gelatin material[23] and is located at a distance t above an array of rectangular shaped PSCs. The material between the PSCs and the CVHLA is assumed to be glass with a refractive index of 1.5, but it can also be PMMA, air, or any other transparent material.

The band gap energy, conversion efficiency, and spectral conversion efficiency (SCE) of the PSCs (Table 1) are taken from the literature and are based on experimental data. The SCE is calculated from the reported values for the external quantum efficiency (EQE), fill factor (FF), and open circuit voltage (V_{OC}) using the following equation:[1]

$$\mathrm{SCE}(\lambda) = V_{\mathrm{oc}} \cdot \mathrm{FF} \cdot \frac{q\lambda}{hc} \cdot \mathrm{EQE}(\lambda). \tag{1}$$

Although this equation is defined for a one-sun illumination condition, it can be used for low-concentration illumination conditions with minimal error. The conversion efficiency of a PSC may even increase slightly for low illumination levels by adjusting the absorber thickness.[24] In the system described in this paper, PSC I has a band gap of 2.30 eV and a conversion efficiency of 10.4%,[2] PSC II has a band gap of 1.63 eV and a conversion efficiency of 21.6%,[3] and PSC III

Table 1 List of perovskite PV cells.

PV cell index	Perovskite cell type	Bandgap (eV)	Spectral band	Published efficiency (%)
I	$CH_3NH_3PbBr_3$ perovskite[2]	2.30	0.300 μm < $\lambda \le$ 0.535 μm	10.4[2]
II	Rubidium cation perovskite[3]	1.63	0.535 μm < $\lambda \le$ 0.760 μm	21.6[3]
III	Sn-Pb perovskite[4]	1.25	0.760 μm < $\lambda \le$ 1.050 μm	20.4[4]

has a band gap of 1.25 eV and a conversion efficiency of 20.4%.[4] Each PSC is assumed to be electrically independent. The SCE of each PSC is shown in Fig. 2(b). The spectral bands for PSCs I, II, and III are defined based on the band gap energies as $0.300\ \mu\text{m} < \lambda \leq 0.535\ \mu\text{m}$, $0.535\ \mu\text{m} < \lambda \leq 0.760\ \mu\text{m}$, and $0.760\ \mu\text{m} < \lambda \leq 1.050\ \mu\text{m}$, respectively.

With ideal optical filters, this combination of PSCs could reach a conversion efficiency of 31.5% in an SSPV system as calculated using the method described by Russo et al.[1] However, the spectral separation of the CVHLA is not ideal and must be evaluated using a detailed model to determine the conversion efficiency that can be realized with this design. In this paper, the optical design of the CVHLA is presented first. Next, a spectral diffraction efficiency model for cascaded VHLs is developed and experimentally verified. Finally, the model is used to analyze the optical losses and their effect on the overall hypothetical conversion efficiency. From this model, it is calculated that the optical losses would reduce the conversion efficiency from 31.5% to 26.7%.

2 Cascaded Volume Holographic Lens Array

The CVHLA consists of two vertically stacked VHL arrays (Fig. 3). The upper VHL array is denoted as layer A, and the lower VHL array is denoted as layer B. Each hologram array consists of six different VHLs with dimensions that match the solar cells underneath them. The spectral diffraction range and diffraction angles of each VHL are selected to achieve optimal spectral separation between the PV cells. The VHL in the upper layer diffracts light in one of the three spectral bands towards a PV cell with the corresponding spectral conversion range (e.g., spectral band I is diffracted toward PV cell I). In a similar approach, the hologram in the lower layer diffracts light in one of the other two spectral bands toward a PV cell with the matching spectral conversion range. This leaves the final spectral band to be transmitted directly to the underlying PV cell without diffraction. The selection of the two diffracted spectral bands ensures that the transmitted spectrum matches the spectral conversion range of the underlying cell.

Each VHL has several design parameters which must be selected to implement the spectral separation described above. Each VHL has a transition wavelength, $\lambda_{T,I}$ or $\lambda_{T,II}$, which corresponds to the band gap energy of PV cell I or II. Light at the transition wavelength comes to a focus at an intersection R_f between two PV cells as discussed in further detail later in this section. Incident solar illumination with a wavelength longer than the transition wavelength is dispersed across the PV cell with the narrower band gap and shorter wavelength light is dispersed across the PV cell with the wider band gap. The specific transition wavelength is selected based on the energy band gaps of the two adjacent PV cells. For example, if the two adjacent cells are PV cells I and II, then the transition wavelength $\lambda_{t,I} = 0.535\ \mu\text{m}$ is selected to provide a sharp transition between spectral bands I and II. In the case where the adjacent cells are PV cells II and III, the transition wavelength $\lambda_{t,II} = 0.760\ \mu\text{m}$ is selected. In addition to the transition wavelength, each VHL also has a Bragg wavelength λ_B. The Bragg wavelength is selected to match the diffracted wavelengths with the spectral conversion range of the target PV cell. For example, a VHL diffracting light toward PV cell III may have a Bragg wavelength $\lambda_B = 0.850\ \mu\text{m}$ to maximize diffraction efficiency in spectral band III and have a transition wavelength $\lambda_{T,II} = 0.760\ \mu\text{m}$ to provide a sharp spectral cutoff between spectral bands II and III.

There are several alternative combinations of the design parameters λ_T, R_f, and λ_B that can accomplish lateral spectral separation. The combination used in this paper is selected for

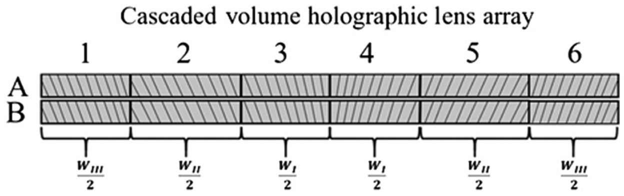

Fig. 3 A cascaded VHL array used in a three-band gap lateral spectrum-splitting module. The numbers 1 to 6 denote the VHL indices, and A and B denote the VHL layer.

minimizing the optical losses which are described in greater detail in Sec. 4. One of the losses that occurs when using cascaded holograms is cross-coupling, which reduces the diffraction efficiency of the primary diffraction order and results in reduced power conversion efficiency (PCE).[25–27] Cross-coupling is an effect that occurs when light diffracted by a hologram in the upper layer is subsequently diffracted by a hologram in the lower layer. Cross-coupling is mitigated by minimizing the overlap between the diffracted spectral and angular bands of the upper hologram and the spectral and angular acceptance bands of the lower hologram. The simplest way to accomplish this is to design the cascaded VHL pair to diffract light in opposite (right/left) directions.[28] This approach is used in the CVHLA design to reduce the cross-coupling.

The illustration in Fig. 4 shows the mapping between spectral bands and PV cells for each VHL. The colors of the arrows represent the different spectral bands, and the directions of the arrows show which PV cell the VHL is designed to diffract to. In Fig. 4(a), the diffracted spectral bands for VHLs 1 and 6 are shown. These VHLs are located at the edges of the unit cell. Light incident on the upper VHL (element 6, layer A) is diffracted in the green spectral band (II: $0.535\ \mu\text{m} < \lambda \leq 0.760\ \mu\text{m}$) and directed toward the left side of the unit cell. The lower VHL (element 6, layer B) diffracts light in the blue spectral band (I: $0.300\ \mu\text{m} < \lambda \leq 0.535\ \mu\text{m}$) toward the right side of the unit cell. This configuration reduces cross-coupling since each element diffracts in opposite directions. VHLs 2 and 5 are shown in Fig. 4(b) and, unlike the VHLs just described, do not diffract in opposite directions. For this pair of VHLs, a more important consideration is the suppression of higher order diffraction since, for a hologram diffracting light in spectral band III, the second-order diffraction resonance occurs in the same wavelength

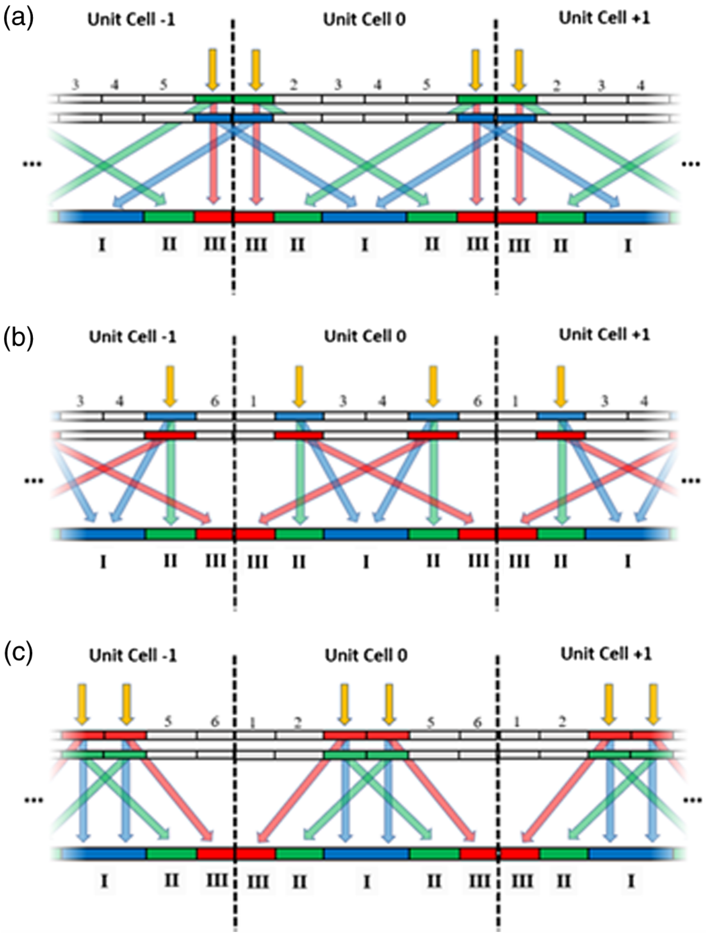

Fig. 4 Illustration depicting the target PV cell and spectral band for each VHL. Neighboring unit cells are also shown. Blue colored arrows indicate spectral band I, green colored arrows indicate spectral band II, and red colored arrows indicate spectral band III. (a) VHLs 1 and 6. (b) VHLs 2 and 5. (c) VHLs 3 and 4.

range as spectral band I. The upper VHL is selected to diffract light in spectral band I, and the lower VHL is selected to diffract light in the red spectral band (III: $0.760\ \mu\text{m} < \lambda \leq 1.050\ \mu\text{m}$). This arrangement suppresses higher-order diffraction by reducing the overlap between the transmitted zeroth-order of the upper VHL and the spectral diffraction range of the second-order of the lower VHL. There is still sufficient angular and spectral separation for this configuration to suppress most of the cross-coupling due to the greater difference in wavelength between spectral bands I and III. Lastly, VHLs 3 and 4 are shown in Fig. 4(c) and, like elements 1 and 6, diffract light in opposite directions to minimize cross-coupling.

An illustration of the transition wavelengths and focus positions for each VHL is shown in Fig. 5. The cyan-colored light indicates that the VHL has a transition wavelength of $\lambda_{t,I}$, and the yellow light indicates the VHL has a transition wavelength of $\lambda_{t,II}$. The point R_f for each VHL is located where the diffracted beam comes to a focus and is marked by an orange dot. VHLs 1 and 6 are shown in Fig. 5(a), and both have a transition wavelength equal to $\lambda_{t,I}$. For each of these elements, the position R_f is located between PV cells I and II. VHLs 2 and 5 are shown in Fig. 5(b). The VHL in the upper layer has a transition wavelength of $\lambda_{t,I}$, and a focus position R_f between PV cells I and II. The VHL in the lower layer has a transition wavelength of $\lambda_{t,II}$, and a focus position R_f between PV cells II and III. VHLs 3 and 4 are shown in Fig. 5(c). The VHL in the upper layer has a transition wavelength of $\lambda_{t,II}$, and a focus position R_f between PV cells II and III. The VHL in the lower layer has a transition wavelength of $\lambda_{t,I}$, and a focus position R_f between PV cells I and II.

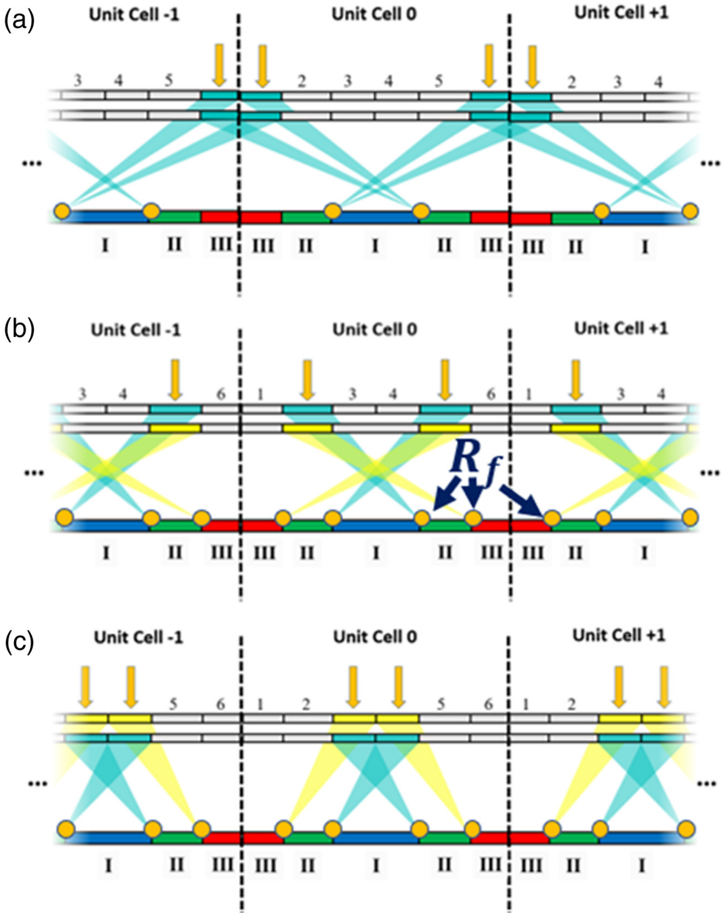

Fig. 5 Illustration showing the transition wavelength and focus position for each VHL. Neighboring unit cells are also shown. The cyan light indicates the transition wavelength $\lambda_{T,I}$ and the yellow light indicates the transition wavelength $\lambda_{T,II}$. Each point that the beam comes to a focus is a focus position R_f and is marked by an orange dot. (a) VHLs 1 and 6. (b) VHLs 2 and 5. (c) VHLs 3 and 4.

The parameters λ_T, R_f, and λ_B are used to determine an optimal pair of point sources for constructing the holographic lenses. Since the reconstruction wavelengths differ from the laser construction wavelength (0.532 μm), there is no exact solution for the point sources. Accordingly, the positions of the construction point sources for each VHL are optimized using a numerical method.[19]

The final two VHL parameters are the holographic film thickness d and index modulation n_1. The film thickness determines the spectral bandwidth of the hologram. In general, thicker volume holograms have narrower bandwidths, and thinner holograms have wider bandwidths. However, if the film thickness is too thin, other issues occur such as significant diffraction in higher orders or index modulation that exceeds the capability of the material. For this design, the film thickness values were determined through simulation and optimization to balance and minimize the various optical losses, which are described in Sec. 4. After choosing the film thickness, the index modulation is selected for maximizing the diffraction efficiency of light with wavelength λ_B. The film thickness and index modulation values are selected within ranges ($2\ \mu\text{m} \le d \le 30\ \mu\text{m}$, $0.01 \le n_1 \le 0.10$) that can be manufactured in the dichromated gelatin material.[23]

The CVHLA parameters are listed in Table 2. The dimensions of the VHLs were selected assuming a distance between the hologram and the PV cells of $t = 10$ mm and a total unit cell width of $w_u = 10$ mm. The dimensions of the unit cell can be scaled without affecting the hypothetical conversion efficiency or the simulated optical loss analysis in the proceeding sections. The VHL widths, PSC widths, and VHL construction point sources should be scaled proportionately, but the film thickness and index modulation values should not change from the initial design values listed in Table 2. In practice, the differences in the implementation of the SSPV system at different scales will affect the conversion efficiency. In this design, it is assumed that the cells are directly adjacent to each other without any separation gap. However, slot-die coating deposition techniques leave a gap of ∼1 mm between the cells.[15] Some of the incident light will be diffracted toward the gap region and reduce the irradiance converted by the solar cells. For this reason, the PCE measured in practice will be lower than the simulated values. This effect could be mitigated by scaling the dimensions of the design so the gap area accounts for a lower proportion of the overall cell area. Other optical techniques could be designed to mitigate the loss, such as the implementation of diffuse or reflective, holographic surfaces.[29]

3 Modeling a Cascaded Volume Holographic Lens

Although the CVHLA model above was designed to mitigate cross-coupling, this effect cannot entirely be eliminated. Therefore, an accurate model of the diffraction efficiency must include the effect of cross-coupled light. In this section, a diffraction efficiency model for cascaded VHLs is developed that extends approaches found in literature. Existing models calculate the cross-coupling between the primary diffraction orders of the upper and lower holograms but do not calculate the efficiency of modes diffracted in a higher order by one or both of the holograms.[25,27] The effect of higher order diffraction cannot be neglected since it accounts for nearly 20% of the optical losses. The model presented in this paper helps address this limitation by calculating the cross-coupled diffraction efficiency between combinations of higher diffraction orders.

The first step in simulating a cascaded volume hologram is to calculate the diffraction efficiency of the upper hologram using rigorous coupled wave analysis (RCWA) techniques as described by Moharam and Gaylord.[30] The diffraction efficiency in the l'th diffraction order of the upper hologram is denoted as $\eta_l(\theta_i, \lambda)$, where θ_i is the angle of incidence, and λ is the wavelength of light. The lower hologram is also simulated using RCWA, but the angle of incidence is set equal to the diffraction angle θ_d of the upper hologram (Fig. 6). The angle θ_d varies as a function of wavelength and diffraction order and is calculated using the grating equation:

$$\sin[\theta_d] = \sin[\theta_i] - \frac{K_x}{2 \cdot \pi \cdot n/\lambda} \cdot l, \tag{2}$$

Table 2 Table of parameters for the cascaded VHL array. The construction point sources R_1 and R_2 are referenced relative to the center of the VHL and assume a construction wavelength $\lambda_c = 0.532$ μm. The parameters listed assume a distance between the hologram and PV cells $t = 10$ mm.

		VHL number					
		1	2	3	4	5	6
A	λ_B (μm)	0.650	0.425	0.850	0.850	0.425	0.650
	λ_T (μm)	0.535	0.535	0.760	0.760	0.535	0.535
	R_f	<1.25 mm, 10.00 mm>	<1.25 mm, 10.00 mm>	<−3.75 mm, 10.00 mm>	<3.75 mm, 10.00 mm>	<1.25 mm, 10.00 mm>	<−1.25 mm, 10.00 mm>
	R_1	<5.08 mm, 7.78 mm>	<3.83 mm, 11.60 mm>	<−3.13 mm, 11.10 mm>	<3.13 mm, 11.10 mm>	<3.83 mm, 11.60 mm>	<−5.08 mm, 7.78 mm>
	R_2	<6.06 mm, 102.00 mm>	<−10.5 m, 318.0 m>	<−3.26 mm, 50.90 mm>	<3.26 mm, 50.90 mm>	<−10.5 m, 318.0 m>	<−6.06 mm, 102.00 mm>
	d (μm)	6	8	30	30	8	6
	n_1	0.049	0.027	0.014	0.014	0.027	0.049
	w (mm)	1.25	2.50	1.25	1.25	2.50	1.25
B	λ_B (μm)	0.450	0.850	0.650	0.650	0.850	0.450
	λ_T (μm)	0.535	0.760	0.535	0.535	0.760	0.535
	R_f	<−11.25 mm, 10.00 mm>	<3.75 mm, 10.00 mm>	<1.25 mm, 10.00 mm>	<−1.25 mm, 10.00 mm>	<3.75 mm, 10.00 mm>	<11.25 mm, 10.00 mm>
	R_1	<−7.46 mm, 12.40 mm>	<6.29 mm, 11.20 mm>	<1.86 mm, 8.92 mm>	<−1.86 mm, 8.92 mm>	<6.29 mm, 11.20 mm>	<7.46 mm, 12.40 mm>
	R_2	<15.6 m, 335.0 m>	<7.13 mm, 58.90 mm>	<1.89 mm, 92.10 mm>	<−1.89 mm, 92.10 mm>	<7.13 mm, 58.90 mm>	<−15.6 m, 335.0 m>
	d (μm)	2	8	30	30	8	2
	n_1	0.100	0.049	0.010	0.010	0.049	0.100
	w (mm)	1.25	2.50	1.25	1.25	2.50	1.25

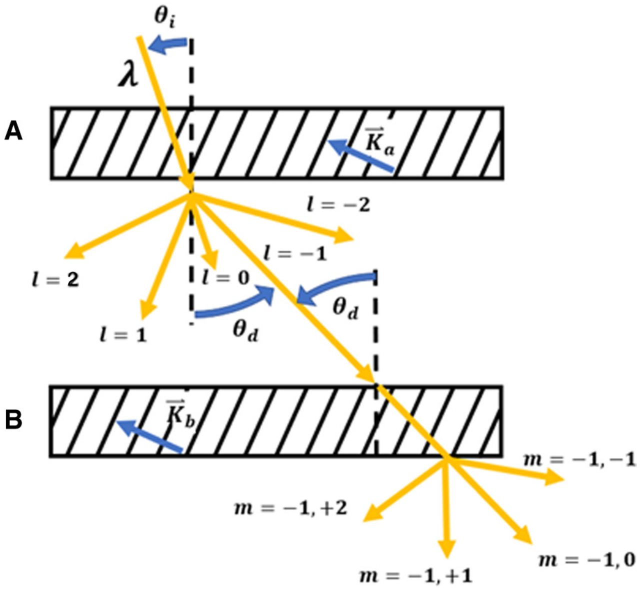

Fig. 6 Illustration of the diffraction orders and geometry in a cascaded hologram. The angle of light diffracted by the upper hologram is equal to the angle of incidence of the lower hologram.

where K_x is the lateral component of the grating vector, and n is the index of refraction. The diffraction efficiency of the lower hologram in the k'th diffraction order is denoted as $\eta_k(\theta_d, \lambda)$ and is calculated by inserting Eq. (2) into the argument of η_k:

$$\eta_k(\theta_d, \lambda) = \eta_k\left(\arcsin\left[\sin[\theta_i] - \frac{K_x}{2 \cdot \pi \cdot n/\lambda} \cdot l\right], \lambda\right). \tag{3}$$

The combined diffraction efficiency of the cascaded hologram $\eta_m(\theta_i, \lambda)$ can now be calculated where $m = l, k$ is the light diffracted in order l by the upper hologram and subsequently diffracted in order k by the lower hologram. This value is obtained by multiplying $\eta_l(\theta_i, \lambda)$ by Eq. (3):

$$\eta_m(\theta_i, \lambda) = \eta_l(\theta_i, \lambda) \cdot \eta_k\left(\arcsin\left[\sin[\theta_i] - \frac{K_x}{2 \cdot \pi \cdot n/\lambda} \cdot l\right], \lambda\right). \tag{4}$$

The diffraction model is verified experimentally by measuring the diffraction efficiency of a cascaded volume hologram. The individual holograms are constructed by exposing 16-μm-thick Covestro Bayfol HX photopolymer film[31] with light from a 0.457-μm DPSS laser. The upper hologram is formed with beams at angles of 0 deg and 30 deg, and the lower hologram is formed with beams at angles of 0 deg and 25 deg. The photopolymer is exposed with an energy dosage of 8.4 $\mathrm{J/cm^2}$ and then cured by exposing the film to sunlight for more than 5 min. After curing the photopolymer, the diffraction efficiency is measured using a Thorlabs power meter and is adjusted to account for surface reflections from the glass substrate.[18,28]

First, the diffraction efficiency of the upper and lower holograms is measured separately and compared with the computed RCWA diffraction efficiency. The RCWA model is implemented in Python[19] and assumes each hologram is formed with the construction angles specified in the previous paragraph, has a film thickness of 16 μm, and has an index modulation of 0.01. The experimental diffraction efficiency of the individual holograms and the computed RCWA diffraction efficiency are in close agreement (Fig. 7). Next, the upper hologram is placed in contact with the substrate of the lower hologram to form a cascaded hologram (Fig. 8). The gap between the two holograms is filled with an index matching fluid to reduce surface reflections. The diffraction efficiency of the cascaded hologram is measured as a function of incidence angle for the $m = +1, 0$, $m = 0, +1$, $m = 0, 0$, and $m = +1, -1$ orders. The diffraction efficiency of the cascaded hologram pair is measured experimentally and then compared with the

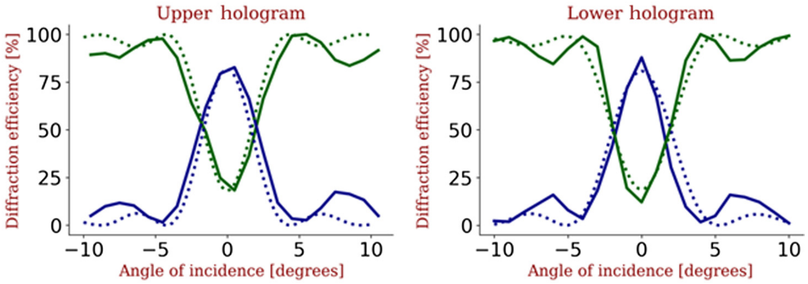

Fig. 7 Individually measured (solid line) and computed (dotted line) diffraction efficiencies for the upper and lower holograms.

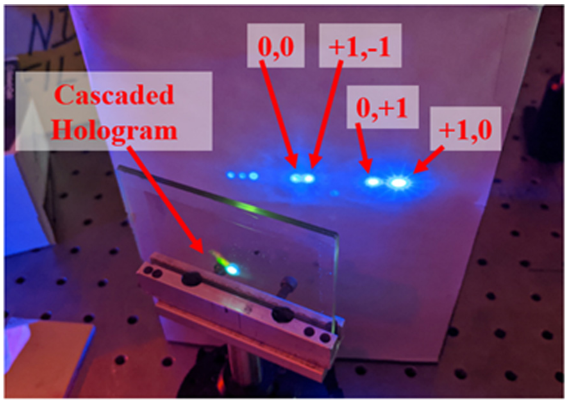

Fig. 8 Picture of a cascaded hologram diffracting light into several orders. The orders that are identified in the text blocks are measured and plotted in Fig. 9. The other orders that are visible but not identified are the $m = -1{,}0$, $m = 0, -1$, $m = -2, +1$ orders and have <1% diffraction efficiency. The laser wavelength is 0.457 μm and the energy exposure density is 8.4 J/cm^2. The upper and lower holograms both have a film thickness of 16 μmand an index modulation of 0.01. The grating period of the upper hologram is 0.91 μm and is 1.08 μm for the lower hologram.

RCWA model for cascaded holograms [Eqs. (1)–(3)]. The measured and computed diffraction efficiencies are plotted in Fig. 9. The error is quantified by taking the absolute difference between the measured and computed curves and averaging between −10 deg and 10 deg. The error for each of the diffracted orders ($m = +1{,}0$, $m = 0, +1$, $m = +1, -1$) is <5% and the error for the transmitted order ($m = 0{,}0$) is <10%. In addition to the diffraction orders plotted in Fig. 9, the $m = -1{,}0$, $m = 0, -1$, and $m = -2, +1$ orders are also visible in Fig. 8. These orders were not measured as a function of angle of incidence, but it was confirmed that the diffraction efficiency did not exceed 1%.

This method is suitable for computing the diffraction efficiency of a uniform cascaded hologram stack in which each hologram has a constant grating period. However, in the CVHLA, the grating period is modulated across the element to provide focusing. Since the RCWA model is only applicable for a constant grating period,[30] the CVHLA is divided into L different segments that are each locally approximated as a uniform cascaded hologram with diffraction efficiency calculated using Eq. (4). This approach is based on the method implemented by Luo et al. for single-layer VHLs[32] but is extended here for application to cascaded VHLs.

The diffraction efficiency of the CVHLA is computed using this approach. The spatial variation is simulated by dividing the element into 120 segments along the aperture of the unit cell. The individual diffraction efficiency of the upper VHLs is plotted in Figs. 10(a)–10(c) without accounting for any interactions with the lower VHLs. Likewise, the diffraction efficiency of the lower VHLs is plotted in Figs. 10(d)–10(f). The results in the plot are obtained by averaging the computed spectral diffraction efficiency for each segment of the VHL. Each of the VHLs has a resonance in either the +1 or −1 diffraction order (the −1 order diffracts toward the right and

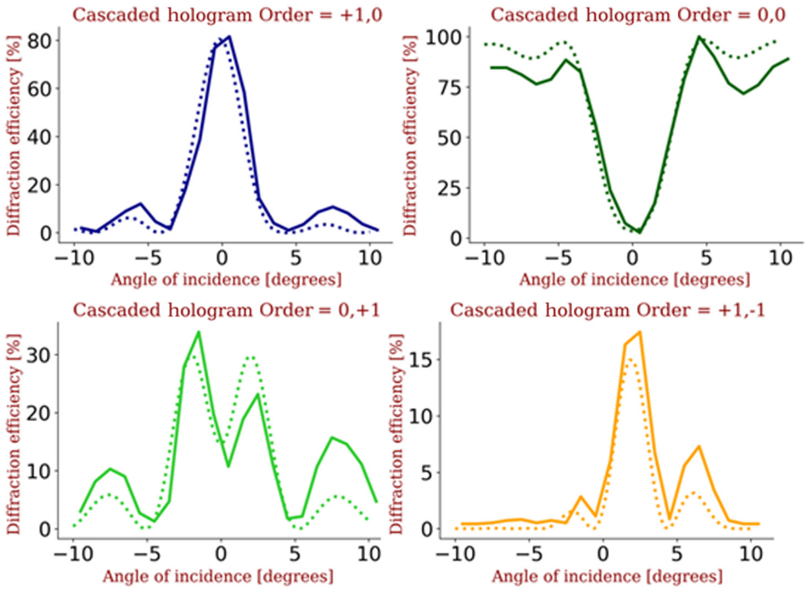

Fig. 9 Measured (solid) and computed (dotted) diffraction efficiencies of a cascaded volume hologram.

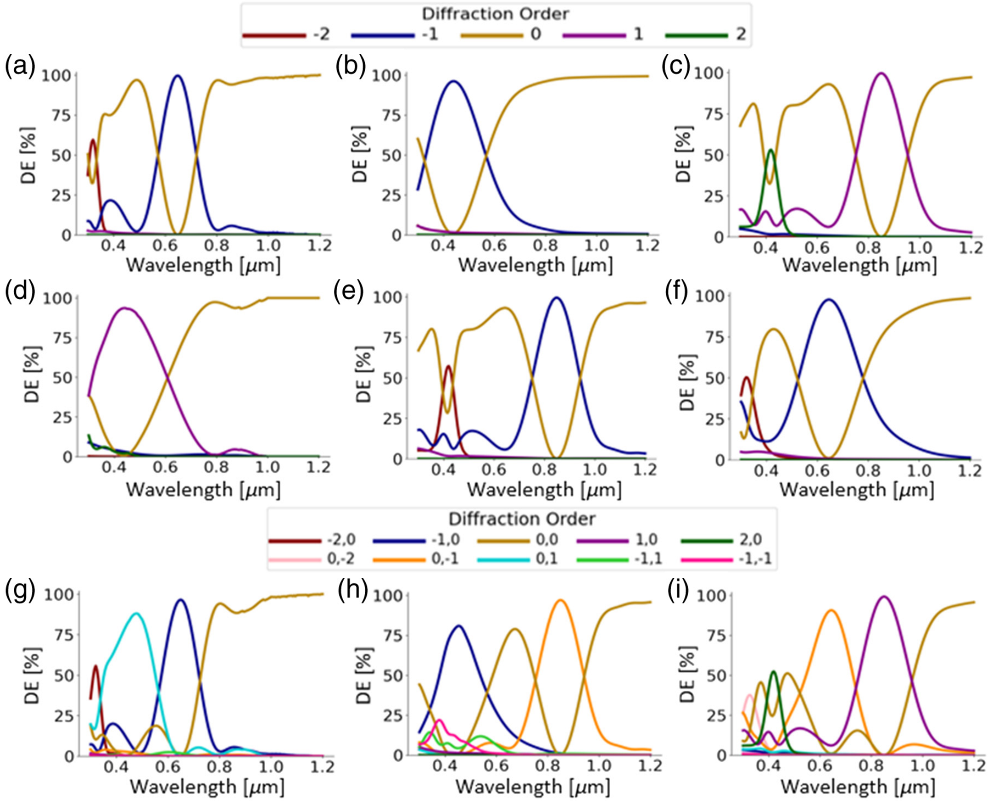

Fig. 10 Plot of the spectral diffraction efficiencies for individual and cascaded hologram layers. (a) Upper layer A VHL 1, (b) upper layer A VHL 2, (c) upper layer A VHL 3, (d) lower layer B VHL 1, (e) lower layer B VHL, 2 (f) lower layer B VHL 3, (g) cascaded VHL 1, (h) cascaded VHL 2, and (i) cascaded VHL 3. Since the CVHLA is symmetrical, the diffraction efficiency of VHLs 1, 2, and 3 are equal to the oppositely signed diffraction orders of VHLs 6, 5, and 4, respectively. For example, the spectral diffraction efficiency of VHL 5 in order $m = -1{,}0$ is equal to VHL 2 in order $m = +1{,}0$.

the +1 order diffracts toward the left). As expected from the initial design, the resonance occurs in one of the three spectral bands corresponding to the different PV cell energy band gaps.

The spectral diffraction efficiency after cascading the VHLs is then plotted in Figs. 10(g)–10(i). Since the upper and lower holograms each diffract in a different spectral band, the cascaded hologram has two primary resonance peaks. Each of the primary resonance peaks corresponds to the $m = +1{,}0$, $m = -1{,}0$, $m = 0, +1$, or $m = 0, -1$ diffraction order. In addition to the primary diffraction orders, light is also diffracted into cross-coupled modes and higher order modes. Compared with other VHLs, holograms 1 and 6 [Fig. 10(g)] have the least diffracted power in cross-coupled or higher order modes. Conversely, cascaded VHLs 2 and 5 [Fig. 10(h)] have greater diffraction efficiency in cross-coupled modes ($m = -1, -1$; $m = -1, +1$). Lastly, cascaded VHL pairs 3 and 4 [Fig. 10(i)] have little power diffracted in cross-coupled orders but have the greatest parasitic loss from higher order modes ($m = +2{,}0$; $m = 0, -2$).

4 System Analysis

After computing the diffraction efficiency, a ray trace simulation is used to calculate the spectral flux on the surface of the PV cells. This method is selected for versatility and the availability of literature describing related approaches.[18,19] The effect of different optical losses that reduce the conversion efficiency of the PV system is then analyzed.

The ray trace simulation is implemented in Python. Rays are created at 100 different starting positions across the aperture of the unit cell and for 50 different wavelengths. The rays are assumed to intersect the CVHLA at normal incidence, and the direction of diffraction is computed using the grating equation. The flux of each ray is then weighted by the diffraction efficiency as computed in the previous section. After tracing the rays to the surface of the PV cells, each diffracted ray is sorted into one of the three different spectral bands and plotted as a spatial distribution in Fig. 11(a). The horizontal axis corresponds to the position on the PV cell plane and is normalized to the unit cell width (+0.5 is the right edge of the unit cell, and −0.5 is the left edge). The blue, green, and red colored background indicates the position of PV cells I, II, and III, respectively. Ideally, each spectral band diffracted by the CVHLA is directed to the corresponding PV cell. For example, all flux in spectral band I should be located on PV cell I without any flux reaching PV cells II or III. The spatial distribution validates the CVHLA design by showing that most of the light within each spectral band reaches the intended PV cell. Sharp transitions between spectral bands are observed on the edges of the PV cells and validate the selection of the transition wavelengths and focal positions. However, it is also observed that some of the flux is directed to unintended solar cells. The source of this misallocated light is analyzed in the following discussion.

To analyze the sources of the misallocated light, each ray is sorted based on the diffraction order from the CVHLA. The spatial distribution of light from the primary diffraction order is plotted in Fig. 11(b). Most of this light reaches the intended PV cell but some is diffracted across the edge to an adjacent PV cell. Losses from the main diffraction order are classified as dispersion losses since they occur when light from the main order is dispersed onto a nonoptimal solar cell. An example of the dispersion loss is observed in Fig. 11(b) where spectral band I leaks across the edge of PV cell I and onto PV cell II. Next, the light that is transmitted without diffraction ($m = 0, 0$) is plotted in Fig. 11(c). As described previously, the VHL is designed to transmit one of the three spectral bands to the underlying PV cell without diffraction. This aspect of the design is evident in Fig. 11(c), since the flux in each spectral band is greatest inside the corresponding PV cells. However, some of the light that is ideally diffracted to a different PV cell is instead transmitted to the underlying cell. This loss is classified as a low diffraction efficiency loss. The low diffraction efficiency loss results from nonuniform spectral diffraction efficiency (Fig. 10) and from the variation of diffraction efficiency across the VHL aperture. The spatial distribution of light from the cross-coupled orders is plotted in Fig. 11(d). As mentioned previously, cross-coupling can significantly reduce the flux reaching the intended solar cells. However, the effect shown here is relatively small since it was specifically addressed in the design of the CVHLA. Lastly, the spatial distribution of light diffracted into higher orders (l and k up to the third order) is shown in Fig. 11(e). Very little light from the higher order

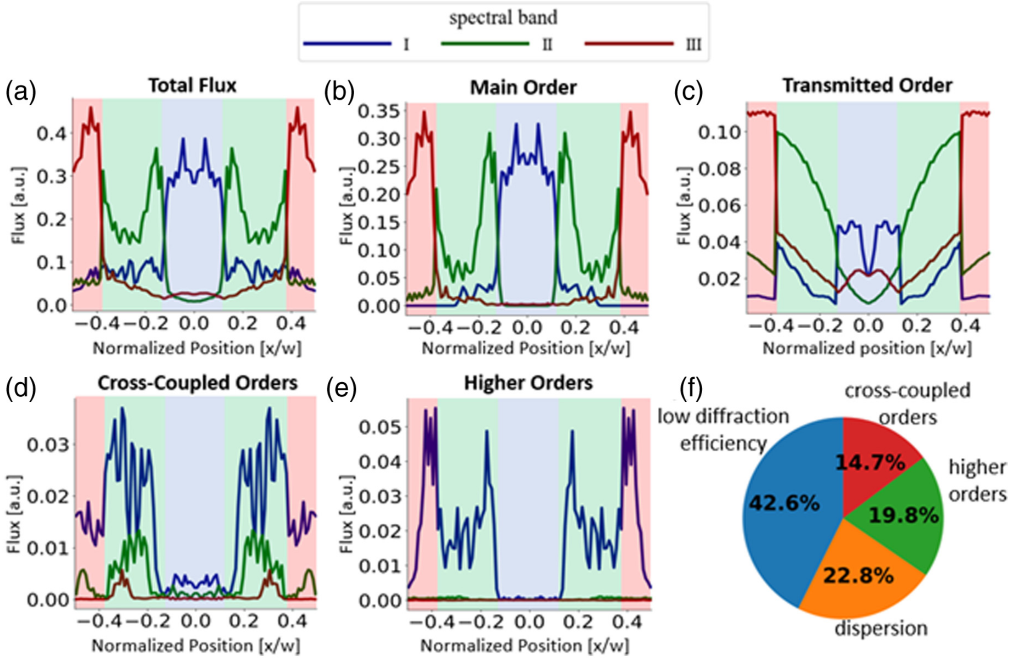

Fig. 11 Plot of the spatial distribution of light on the surface of the PV cells for spectral bands I, II, and III. The fluxes from the different diffraction orders are plotted separately. The color of the background indicates the position of each PV cell. The horizontal axis is the position along the unit cell and is normalized to the total width of the unit cell. The ray flux is plotted on the vertical axis and is reported in arbitrary units. (a) Total flux from all diffracted orders. (b) Light that is diffracted in a primary order. (c) Light that is transmitted without being diffracted. (d) Light that is cross-coupled. (e) Light that is diffracted in a higher order. (f) Pie chart indicating the percentage of optical losses caused by low diffraction efficiency, cross-coupled light, dispersion, and higher order diffraction.

modes reach the intended PV cells. 97% of the light diffracted in a higher order mode is in spectral band I and is distributed across PV cells II and III. The reason most of the higher-order diffraction is in spectral band I is because higher-order modes have resonances at shorter wavelengths.[33]

The relative contribution of each loss is shown as a fraction of the total loss in the pie chart in Fig. 11(f). The relative loss is calculated by dividing the misallocated flux for a given diffraction order by the total misallocated flux. The greatest loss is low diffraction efficiency (42.6%) followed by dispersion (22.8%), higher orders (19.8%), and cross-coupled orders (14.7%).

The optical loss analysis above assumes normally incident sunlight and perfect alignment between the hologram and the PV cells. In practice, these conditions will not be perfectly met and will reduce the conversion efficiency of the system. The diffraction efficiency of a volume hologram is primarily sensitive to the in-plane angle of incidence. The design in this paper assumes implementation with a single-axis sun tracking system such that the angle of incidence lies in the plane of the grating vector. In this arrangement, the out-of-plane incidence angle varies between -23.45 deg and $+23.45$ deg throughout the course of the year. However, the diffraction efficiency remains high within this range, and the average conversion efficiency is only reduced by a fraction of a percent.[19,28,34] Vertical misalignment (i.e., the distance t) reduces the isolation of the cutoff between spectral bands since, in this case, sunlight at the transition wavelength does not come to a focus between solar cells as intended in the design. However, the peak diffraction efficiency occurs for wavelengths in the center of the spectral band which are further from the transition wavelength and dispersed further away from the edges of the PV cell. Therefore, the sensitivity to vertical misalignment may be tolerable within deviations of several percent.

Next, the spectral optical efficiency $\mathrm{SOE}(\lambda)$ of the system is calculated. First, the spectrum incident on the j'th PV cell $E_j(\lambda)$ is calculated by summing the flux on each PV cell as a function

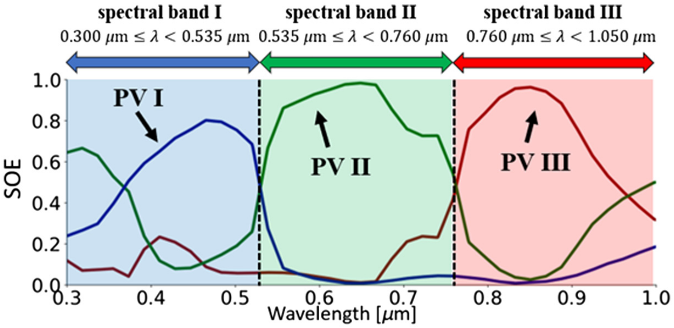

Fig. 12 Plot of the spectral optical efficiency showing the fraction of light reaching each PV cell as a function of wavelength. The optimal spectral bands are shown by the colored arrows on the top.

of wavelength. The $\mathrm{SOE}_j(\lambda)$ is then calculated by dividing $E_j(\lambda)$ by the total incident direct solar spectrum $\mathrm{AM1.5}D(\lambda)$[35] illuminating the unit cell:

$$\mathrm{SOE}_j(\lambda) = \frac{E_j(\lambda)}{\mathrm{AM1.5}D(\lambda)}. \tag{5}$$

The $\mathrm{SOE}(\lambda)$ is plotted in Fig. 12 and shows clear transitions between spectral bands at wavelengths $\lambda = 0.535\ \mu\mathrm{m}$ and $\lambda = 0.760\ \mu\mathrm{m}$. The $\mathrm{SOE}(\lambda)$ for PV cell I is lower than other PV cells since more flux is diffracted in higher orders or cross-coupled orders at shorter wavelengths.

The PCE for direct normally incident sunlight is obtained by multiplying the solar spectrum $\mathrm{AM1.5}D(\lambda)$ by the $\mathrm{SOE}_j(\lambda)$ and the $\mathrm{SCE}_j(\lambda)$ for the j'th cell, integrating over all wavelengths, and summing the contributions from each PV cell:[1,19]

$$\mathrm{PCE} = \sum_j \frac{\int \mathrm{AM1.5}D(\lambda) \cdot \mathrm{SOE}_j(\lambda) \cdot \mathrm{SCE}_j(\lambda) \cdot \mathrm{d}\lambda}{\int \mathrm{AM1.5}D(\lambda) \cdot \mathrm{d}\lambda}. \tag{6}$$

The PCE for diffuse sunlight is calculated using a modified form of Eq. (6) by replacing the direct solar spectrum with the diffuse solar spectrum $\mathrm{AM1.5}F(\lambda)$, which is defined here as the difference between the global $\mathrm{AM1.5}G(\lambda)$ and direct $\mathrm{AM1.5}D(\lambda)$ spectra:

$$\mathrm{AM1.5}F(\lambda) = \mathrm{AM1.5}G(\lambda) - \mathrm{AM1.5}D(\lambda). \tag{7}$$

The $\mathrm{SOE}_j(\lambda)$ was also modified since the differing angular distribution of diffuse sunlight results in a different spatial distribution on the PV cells. Diffuse light is uniformly incident from 2π steradians above the module. A volume hologram has significant diffraction efficiency within two angular bands corresponding to the two Bragg angles. Light with incidence angles outside the diffraction range passes through the hologram and illuminates the PV cell plane. Diffuse light within the diffraction range of an angular band is diffracted in the direction of the other angular band and vice versa resulting in a very small net change in the angular distribution of light as it passes through the hologram. The effect of diffraction is therefore assumed to be negligible and the spatial distribution on the PV cell plane is assumed to be uniform. The $\mathrm{SOE}_j(\lambda)$ for diffuse sunlight was therefore modeled as the fraction of the PV cell width over the total width of the unit cell:[19]

$$\mathrm{SOE}_j(\lambda) = \frac{W_j}{W_I + W_{II} + W_{III}}. \tag{8}$$

The total PCE is the weighted sum of the direct and diffuse PCE. In the global $\mathrm{AM1.5}G(\lambda)$ solar spectrum,[35] 90% of the total solar irradiance is direct and 10% is diffuse. Therefore, the PCE for the direct spectrum is weighted by 90% and the PCE for the diffuse spectrum is weighted by 10%. Based on this analysis, the overall PCE for the CVHLA spectrum-splitting system is found to be 26.7%.

Table 3 Five different sets of PSCs with conversion efficiency values scaled from the experimental values (set 1).

PSC	Set 1 (%)	Set 2 (%)	Set 3 (%)	Set 4 (%)	Set 5 (%)
I	10.40	10.92	11.44	11.96	12.48
II	21.60	22.68	23.76	24.84	25.92
III	20.40	21.42	22.44	23.46	24.48

The final two aspects of the spectrum-splitting design that are analyzed are the effects of the individual perovskite cell conversion efficiency and the diffraction efficiency of the hologram array on the overall PCE. The first aspect, the individual perovskite cell conversion efficiency, is considered since the rapid advances in perovskite cell technology affect the overall conversion efficiency that can be achieved with spectrum splitting systems. This aspect is analyzed by computing the PCE for five different sets of hypothetical perovskite cells (Table 3) that each have greater conversion efficiency than initially assumed in Table 1. For each hypothetical perovskite cell, the experimentally measured SCE(λ) curve is scaled by a constant factor from the raw data obtained from the literature.[2–4] This scaling step is equivalent to scaling the short circuit current (I_{SC}), open circuit voltage (V_{OC}), or fill factor (FF) of the cell.[1] The second aspect, diffraction efficiency, is considered since the diffraction efficiency that is attainable in theory (~100%)[33] is significantly higher than values attained in manufacturing (85% and 95%).[23,36] In this paper, the maximum diffraction efficiency (MDE) is used as a metric and refers to the diffraction efficiency at the Bragg wavelength λ_B for normally incident light. For the initial design parameters (Table 2), the MDE was nearly 100% (Fig. 10). Here, the MDE is reduced from the initial value by decreasing the index modulation. For example, VHL 3 in layer A has an index modulation of 0.014 (Table 2) corresponding to an MDE of ~100%. An MDE of 80% is obtained by setting the index modulation to a value of 0.010.

The overall PCE is plotted as a function of the MDE for each of the five sets of perovskite cells (Fig. 13, Table 4). The results show minimal degradation (0.3%) in the PCE when reducing the MDE from 100% to 90%. The drop in performance is more than twice as much (0.7%) when

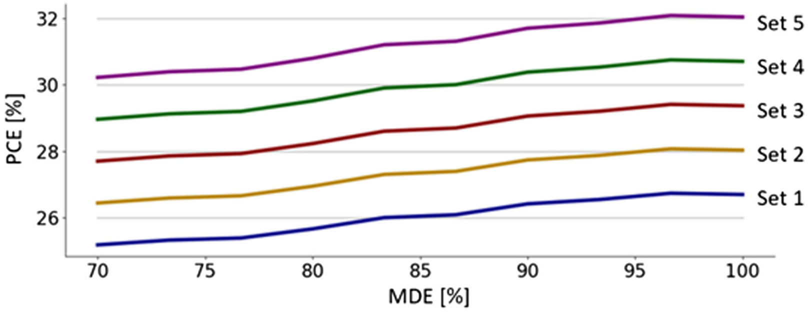

Fig. 13 PCE as a function of the DE for each perovskite cell set listed in Table 3.

Table 4 PCE for different values of the MDE for the perovskite cell sets listed in Table 3.

MDE (%)	Set 1 (%)	Set 2 (%)	Set 3 (%)	Set 4 (%)	Set 5 (%)
80	25.7	27.0	28.2	29.5	30.8
90	26.4	27.7	29.1	30.4	31.7
100	26.7	28.0	29.4	30.7	32.0

the MDE decreases from 90% to 80% and further reduces by 0.5% when the MDE decreases from 80% to 70%. Decreasing the MDE has a different effect on each of the optical losses. Not surprisingly, the low diffraction efficiency losses increase when the MDE decreases from the initial value of 100%. However, the higher-order losses and cross-coupling losses decrease and offset some of the low diffraction efficiency losses. This somewhat counterintuitive behavior occurs since reducing the index modulation also decreases the diffraction efficiency of higher orders and higher harmonics. The overall effect is a nonlinear decrease in conversion efficiency as the diffraction efficiency is decreased. An MDE of 90% avoids the highest rate of degradation between 90% and 80% and is a value that can be achieved in practice. Based on this tolerance analysis, a manufacturing target is to have an MDE greater than 90%.

The final aspect to be discussed is the effect of the individual perovskite cell conversion efficiencies on the overall system conversion efficiency. Figure 13 shows that a set of perovskite cells with individual conversion efficiencies of 12.0%, 24.8%, and 23.5% has potential for attaining a system conversion efficiency of 30.4% when combined with a CVHLA that has a diffraction efficiency greater than 90%. The most efficient PSC on record already has a conversion efficiency of 25.5%[6,7] (small-area, certified) with a band gap (1.55 eV) close to PV cell II (1.63 eV).[3] Significantly less research has been conducted on PSCs with 1.25 and 2.30 eV band gaps. With improvements in the conversion efficiency of PSCs at these band gaps, a lateral spectrum-splitting system with a conversion efficiency greater than 30% may be attainable.

5 Conclusion

In this paper, a lateral SSPV system is proposed that splits sunlight between three PSCs. The design uses a cascaded VHL array for spectral separation. Each VHL has a transition wavelength, focus position, and Bragg wavelength that are specified for attaining sharp transitions between spectral bands. The cascaded holographic array elements are analyzed using RCWA to determine the diffraction efficiency and sources of optical losses. The simulated hologram performance is verified with experimental measurements, and the results agree to within 5%. A combination of optical losses such as low diffraction efficiency, higher order diffraction, dispersion, and cross-coupled orders is shown to contribute to reduced spectral optical efficiency. The spectrum-splitting system was shown to attain a hypothetical conversion efficiency of 26.7% using a set of perovskite cells based on published, experimental results with efficiencies of 10.4%, 21.6%, and 20.4%. It is also shown that a PCE of 30.4% could be realized using perovskite cells with individual conversion efficiencies of 12.0%, 24.8%, and 23.5%, respectively, and using VHLs with high diffraction efficiencies (>90%) that can be achieved in practice.

Acknowledgments

This paper was based on work included in Benjamin Chrysler's PhD dissertation. The authors would like to acknowledge the valuable comments and suggestions from committee members Yuzuru Takashima, Robert Norwood, and Pierre Blanche. The authors would also like to acknowledge support from NSF/DOE ERC Cooperative Agreement No. EEC-1041895, NSF Grant Nos. ECCS-1405619 and DMR-1906029, and NREL partner authorization UGA-0-41026-117. Benjamin Chrysler would like to acknowledge support from the NSF Graduate Research Fellowship Program DGE-1143953. Any opinions, findings, recommendations expressed in this material are those of the authors and do not necessarily reflect the view of the National Science Foundation.

References

1. J. Russo et al., "Spectrum splitting metrics and effect of filter characteristics on photovoltaic system performance," *Opt. Express* **22**(S2), A528–A541 (2014).
2. J. H. Heo, D. H. Song, and S. H. Im, "Planar $CH_3NH_3PbBr_3$ hybrid solar cells with 10.4% power conversion efficiency, fabricated by controlled crystallization in the spin-coating process," *Adv. Mater.* **26**(48), 8179–8183 (2014).

3. M. Saliba et al., "Incorporation of rubidium cations into perovskite solar cells improves photovoltaic performance," *Science* **354**(6309), 206–209 (2016).
4. J Tong et al., "Carrier lifetimes of $>1\ \mu$s in Sn-Pb perovskites enable efficient all-perovskite tandem solar cells," *Science* **364**(6439), 475–479 (2019).
5. Z. Li et al., "Cost analysis of perovskite tandem photovoltaics," *Joule* **2**(8), 1559–1572 (2018).
6. H. Min et al., "Perovskite solar cells with atomically coherent interlayers on SnO_2 electrodes," *Nature* **598**(7881), 444–450 (2021).
7. M. A. Green et al., "Solar cell efficiency tables (version 59)," *Prog. Photovoltaics* **30**(1), 3–12 (2022).
8. G. E. Eperon et al., "Perovskite-perovskite tandem photovoltaics with optimized band gaps," *Science* **354**(6314), 861–865 (2016).
9. R. Lin et al., "Monolithic all-perovskite tandem solar cells with 24.8% efficiency exploiting comproportionation to suppress Sn (II) oxidation in precursor ink," *Nat. Energy* **4**(10), 864–873 (2019).
10. N. N. Lal et al., "Perovskite tandem solar cells," *Adv. Energy Mater.* **7**(18), 1602761 (2017).
11. B. Dou et al., "High-performance flexible perovskite solar cells on ultrathin glass: implications of the TCO," *J. Phys. Chem. Lett.* **8**(19), 4960–4966 (2017).
12. Y. Zhang et al., "Fully solution-processed TCO-free semitransparent perovskite solar cells for tandem and flexible applications," *Adv. Energy Mater.* **8**(1), 1701569 (2018).
13. M. Schultes et al., "Sputtered transparent electrodes (IO: H and IZO) with low parasitic near-infrared absorption for perovskite–Cu (In, Ga) Se_2 tandem solar cells," *ACS Appl. Energy Mater.* **2**(11), 7823–7831 (2019).
14. D. A. Jacobs et al., "Light management: a key concept in high-efficiency perovskite/silicon tandem photovoltaics," *J. Phys. Chem. Lett.* **10**(11), 3159–3170 (2019).
15. R. Patidar et al., "Slot-die coating of perovskite solar cells: an overview," *Mater. Today Commun.* **22**, 100808 (2020).
16. B. Dou et al., "Roll-to-roll printing of perovskite solar cells," *ACS Energy Lett.* **3**(10), 2558–2565 (2018).
17. C. Amruth, M. Pahlevani, and G. C. Welch, "Organic light emitting diodes (OLEDs) with slot-die coated functional layers," *Mater. Adv.* **2**(2), 628–645 (2021).
18. S. D. Vorndran et al., "Off-axis holographic lens spectrum-splitting photovoltaic system for direct and diffuse solar energy conversion," *Appl. Opt.* **55**(27), 7522–7529 (2016).
19. B. D. Chrysler and R. K. Kostuk, "High energy yield bifacial spectrum-splitting photovoltaic system," *Appl. Opt.* **59**(22), G8–G18 (2020).
20. E. D. Aspnes et al., "Volume hologram replicator for transmission type gratings," U.S. Patent 8,614,842 (2013).
21. Z. Song et al., "A technoeconomic analysis of perovskite solar module manufacturing with low-cost materials and techniques," *Energy Environ. Sci.* **10**(6) 1297–1305 (2017).
22. M. Cai, et al., "Cost-performance analysis of perovskite solar modules," *Adv. Sci.* **4**(1), 1600269 (2017).
23. C. G. Stojanoff, "Review of the technology for the manufacturing of large-format DCG holograms for technical applications," *Proc. SPIE* **3011**, 267–278 (1997).
24. D. Tian et al., "Light-intensity and thickness dependent efficiency of planar perovskite solar cells: charge recombination versus extraction," *J. Mater. Chem. C* **8**(36), 12648–12655 (2020).
25. Y. Wu, B. D. Chrysler, and R. K. Kostuk, "Design and fabrication of cascaded dichromate gelatin holographic filters for spectrum-splitting PV systems," *J. Photonics Energy* **8**(1), 017001 (2018).
26. S. Darbe et al., "Simulation and partial prototyping of an eight-junction holographic spectrum-splitting photovoltaic module," *Energy Sci. Eng.* **7**(6), 2572–2584 (2019).
27. G. B. Ingersoll and J. R. Leger, "Optimization of multi-grating volume holographic spectrum splitters for photovoltaic applications," *Appl. Opt.* **55**(20), 5399–5407 (2016).
28. J. M. Castro et al., "Energy collection efficiency of holographic planar solar concentrators," *Appl. Opt.* **49**(5), 858–870 (2010).

29. J. Zhao, B. D. Chrysler, and R. K. Kostuk, "Holographic low concentration optical system increasing light collection efficiency of regular solar panels," *J. Photonics Energy* **11**(2), 027002 (2021).
30. M. G. Moharam and T. K. Gaylord, "Rigorous coupled-wave analysis of planar-grating diffraction," *J. Opt. Soc. Am.* **71**(7), 811–818 (1981).
31. F. K. Bruder, T. Facke, and T. Rolle, "The chemistry and physics of Bayfol HX film holographic optical elements recorded in Bayfol HX photopolymer for solar photovoltaic applications," *Polymers* **9**(12), 472 (2017).
32. Y. Luo et al., "Simulations and experiments of aperiodic and multiplexed gratings in volume holographic imaging systems," *Opt. Express* **18**(18), 19273–19285 (2010).
33. H. Kogelnik, "Coupled wave theory for thick hologram gratings," *Bell Syst. Tech. J.* **48**, 2909–2947 (1969).
34. D. Zhang, J. M. Castro, and R. K. Kostuk, "One-axis tracking holographic planar concentrator systems," *J. Photonics Energy* **1**(1), 015505 (2011).
35. C. Gueymard, "SMARTS2: Simple model of the atmospheric radiative transfer of sunshine: algorithms and performance assessment," NREL 1995, www.nrel.gov.
36. B. D. Chrysler and R. K. Kostuk, "Volume hologram replication system for spectrum-splitting photovoltaic applications," *Appl. Opt.* **57**(30), 8887–8893 (2018).

Benjamin D. Chrysler received his BS in electrical engineering from Colorado State University, Fort Collins, Colorado, USA, in 2015, and his PhD in optical science from the University of Arizona, Tucson, Arizona, USA, in 2021. During graduate school, he studied under the guidance of Professor Raymond K. Kostuk and was a recipient of the NSF Graduate Research Fellowship Program award in 2017.

Sean E. Shaheen is a professor of electrical, computer, and energy engineering and professor by courtesy of physics at the University of Colorado Boulder. He received his PhD in physics from the University of Arizona in 1999. His research is in the areas of photovoltaic, photonic, and neuromorphic materials and devices. He is currently the editor-in-chief of the *Journal of Photonics for Energy*.

Raymond K. Kostuk has a joint professorship with UA's ECE Department and James C. Wyant College of Optical Sciences. He received his PhD in electrical engineering from Stanford University. His primary area of expertise is in holographic concepts, materials, and applications, with over 30 years of experience in that area. He is a fellow of SPIE and Optica.